

A low-communication-overhead parallel method for the 3D incompressible Navier-Stokes equations

Jiabin Xie¹, Jianchao He¹, Yun Bao^{1,2*}, Xi Chen^{2*}

¹School of Aeronautics and Astronautics, Sun Yat-sen University, Guangzhou, China.

²Institute of Fluid Mechanics, Beihang University, Beijing, China.

Abstract

This paper presents a low-communication-overhead parallel method for solving the 3D incompressible Navier-Stokes equations. A fully-explicit projection method with second-order space-time accuracy is adopted. Combined with fast Fourier transforms, the parallel diagonal dominant (PDD) algorithm for the tridiagonal system is employed to solve the pressure Poisson equation, differing from its recent applications to compact scheme derivatives computation (Abide et al. 2017¹) and alternating-direction-implicit method (Moon et al. 2020²). The number of all-to-all communications is decreased to only two, in a 2D pencil-like domain decomposition. The resulting MPI/OpenMP hybrid parallel code shows excellent strong scalability up to 10^4 cores and small wall-clock time per timestep. Numerical simulations of turbulent channel flow at different friction Reynolds numbers ($Re_\tau = 550, 1000, 2000$) have been conducted and the statistics are in good agreement with the reference data. The proposed method allows massively simulation of wall turbulence at high Reynolds numbers as well as many other incompressible flows.

KEYWORDS:

direct numerical simulations, incompressible flows, wall turbulence, high performance computing, parallel diagonal dominant (PDD) algorithm

1 Introduction

Understanding wall turbulence is of great importance for both fundamental physics and engineering applications. Owing to the progress of computing technology and the development of numerical methods, large-scale direct numerical simulation (DNS) of wall turbulence has become feasible. Presently, the numerical methods for DNS of wall turbulence are either spectral method^{3,4,5} or finite

*Corresponding author.

Yun Bao, E-mail: stsb@ mail.sysu.edu.cn

Xi Chen, E-mail: chenxi97@outlook.com

difference method⁶. The spectral method is only suitable for flow simulation with simple boundary conditions, but with high data accuracy hence appreciated much by academic study. In contrast, the finite difference method greatly eases restrictions on boundary conditions and enables the simulation of complex flows⁷ provided with the immersed boundary method. Though not as accurate as spectral code, it has been shown that adequate first- and second-order statistics can be obtained by lower-order finite difference schemes when grid resolution is sufficiently high⁸. However, both methods suffer from the issue that a huge demand for memory and computing power is required which limits the application of DNS for turbulent flows at practically high Reynolds number. Taking a simple geometry wall-flow, i.e. turbulent channel, for example, current available DNS data are mostly in the friction-Reynolds-number range $Re_\tau = 180 - 2000$ ^{4,9,10}, whilst data of higher Reynolds Numbers ($Re_\tau = 4000, 4200, 5200$, and 8000)^{6,5,3,11}, though reported, remain relatively fewer.

The most time-consuming part of a numerical simulation of incompressible flow is to solve the pressure Poisson equation. Among the solving methods (e.g., the multigrid method, the fast multipole method), Gholami et al.¹² show that the fast Fourier Transform (FFT) based direct method is more efficient and accurate. The reason is that, using the FFT technique, the pressure Poisson equation can be decoupled into a series of tridiagonal linear equations, which can be solved by the Thomas algorithm hence saving a lot of computation time. The FFT method has already been applied to numerical simulation of incompressible flows¹³, and recently, applied to large-scale parallel numerical simulation of several turbulent flows such as Rayleigh-Bénard convection and Tayler-Couette flow^{14,15,16,17}.

Note that there are two challenges to implement the large-scale parallelization of the FFT-based direct method, i.e., to improve the parallel efficiency of the multi-dimensional FFT calculation in the multi-dimensional decomposition domain, and to exploit the parallelization potential efficiently for solving tridiagonal systems. To achieve the formal goal, open source libraries for parallel multi-dimensional FFT (e.g., PFFT¹⁸, P3DFFT¹⁹ and 2DECOMP&FFT²⁰) can be used which typically adopts 2D pencil-like domain decomposition for better scalability. Although it unavoidably introduces multiple all-to-all global transpose communications, several optimization methods (e.g. minimizing communication amount and computation-communication overlap) can be applied jointly to ensure the parallel efficiency^{21,22}. However, for the latter goal of solving tridiagonal systems which is implicit in nature, it brings in a challenge to the parallel implementation of FFT-based direct method in a multi-dimensional domain decomposition. The existing practice^{14,17} is to keep the computational domain undecomposed in the implicitly coupling direction by all-to-all data transposes, so that the Thomas algorithm can be used. There are several parallel algorithms to solve tridiagonal systems, including the cyclic doubling method²³, the cyclic reduction method²⁴ and a class of methods based on the idea of divide and conquer^{25,26,27}. Among them, the parallel diagonal dominant (PDD) algorithm proposed by Sun et al.²⁷ is of our interest as it is featured by low communication overhead and high parallel efficiency. When the linear system is diagonal dominant, it can provide an approximate solution with error smaller than machine accuracy.

Although the PDD algorithm has been proposed since the 1990s, its applications in computational fluid dynamics are still limited. Abide et al. (2017)¹ employed the PDD algorithm to address the

computations of compact derivatives and interpolations. It demonstrates that the PDD algorithm not only maintains the accuracy and conservation features but also contributes to a good parallel performance up to 4096 cores. Bao et al. (2017)²⁸ introduced the PDD algorithm to solve the pressure Poisson equation for the 2D Rayleigh-Bénard convection. Recently, Moon et al. (2020)² proved the applicability of the PDD algorithm for non-diagonal dominant systems derived from discretization of incompressible momentum equations. The accuracy of results is found to be determined by the CFL number and the number of grid points in each decomposed block.

This paper aims to develop a highly efficient parallel method for solving the 3D incompressible Navier-Stokes equations and use it to accomplish wall turbulence DNS at high Reynolds numbers. Our approach is based on the projection method with the second-order space-time accuracy, and the main idea is to establish an approximate solver for the pressure Poisson equation, which combines 2D FFTs with the PDD algorithm for the tridiagonal system. Using MPI/OpenMP hybrid model and 2D pencil-like domain decomposition, the resulting code, named by us as PowerLLEL (a Powerful paraLLEL solver for incompressible flows), has a very good parallel performance (demonstrated below). We believe that not only wall turbulence but also other incompressible flows can be simulated efficiently by this method.

This paper is organized as follows. Section 2 introduces the numerical method adopted in this paper for channel flow. Section 3 details the parallel strategy and the efficient implementation of the numerical method for massively parallel simulation. Section 4 presents the computational performance of our code. In Section 5, several DNS cases of channel flow are presented to validate our code. Finally, Section 6 presents the main conclusion and an outlook of future works.

2 Numerical method

One of the canonical wall turbulences is channel flow. As illustrated in Figure 1, the flow between two infinite parallel planes is driven by a unidirectional pressure gradient. In order to simulate the flow in an infinite domain, periodic boundary conditions are used in the streamwise (x) and spanwise (y) directions. A no-slip boundary condition is imposed at the two planes in the wall-normal direction (z). The governing 3D incompressible Navier-Stokes equations are as follows

$$\nabla \cdot \mathbf{u} = 0, \quad (1)$$

$$\frac{\partial \mathbf{u}}{\partial t} + (\mathbf{u} \cdot \nabla) \mathbf{u} = -\nabla p + \frac{1}{Re} \nabla^2 \mathbf{u}, \quad (2)$$

where \mathbf{u} is the velocity vector, p is the pressure, t is time and Re is the Reynolds number.

Considering the flow characteristics and the boundary conditions mentioned above, the Navier-Stokes equations are discretized on a Cartesian grid, uniformly-spaced in the streamwise and spanwise directions and nonuniformly-spaced in the wall-normal direction. The spatial discretization scheme is the standard second-order centered finite difference with a staggered arrangement of velocity and pressure variables, as illustrated in Figure 2. Time advancement is performed with an explicit second-

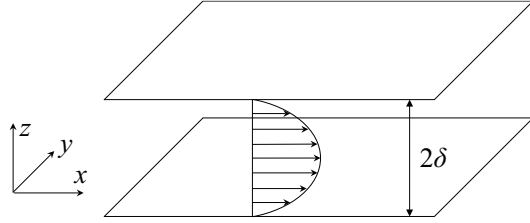


FIGURE 1 Schematic of channel flow. The streamwise, spanwise and wall-normal directions are denoted by x , y and z , respectively. δ is the channel half-height and U is the streamwise mean velocity.

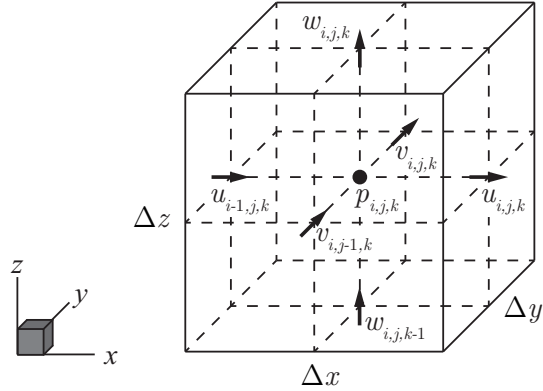


FIGURE 2 Schematic of staggered grids. Velocity vectors are placed at the cell surface while pressure is placed in the cell center.

order Runge-Kutta scheme. Therefore, the projection method used in this paper is as follows.

$$\mathbf{u}^* = \mathbf{u}^n + \Delta t [-N(\mathbf{u}^n) + L(\mathbf{u}^n)], \quad (3)$$

$$\mathbf{u}^{n+1} = \mathbf{u}^* - \Delta t \nabla p^{n+1}, \quad (4)$$

where u^* is the provisional velocity, $N(\mathbf{u}) = (\mathbf{u} \cdot \nabla) \mathbf{u}$ and $L(\mathbf{u}) = \nabla^2 \mathbf{u} / Re$ are the linear and nonlinear terms respectively. The second-order Runge-Kutta scheme is applied to equation (3) to calculate the provisional velocity u^* .

$$\overline{\mathbf{u}^*} = \mathbf{u}^n + \Delta t [-N(\mathbf{u}^n) + L(\mathbf{u}^n)], \quad (5)$$

$$\mathbf{u}^* = \mathbf{u}^n + \frac{1}{2} \Delta t [-N(\mathbf{u}^n) + L(\mathbf{u}^n) - N(\overline{\mathbf{u}^*}) + L(\overline{\mathbf{u}^*})]. \quad (6)$$

The pressure Poisson equation is derived from the combination of the divergence operator with the velocity correction equation (4):

$$\nabla^2 p^{n+1} = \frac{\nabla \cdot \mathbf{u}^*}{\Delta t}. \quad (7)$$

Then p^{n+1} is obtained. The final velocity at the new timestep u^{n+1} can be updated according to equation (4). The velocity boundary conditions should be imposed on the provisional/final velocity at each substep or timestep, while the pressure boundary conditions are imposed only after the pressure Poisson equation is solved.

2.1 The pressure Poisson equation

For the numerical simulation of incompressible flows, the numerical solution of the pressure Poisson equation (7) is often difficult to tackle, because it couples all the points in the three-dimensional domain. For simplicity, consider the following Poisson equation discretized with second-order centered finite difference on a uniform grid:

$$\frac{p_{i-1,j,k} - 2p_{i,j,k} + p_{i+1,j,k}}{\Delta x^2} + \frac{p_{i,j-1,k} - 2p_{i,j,k} + p_{i,j+1,k}}{\Delta y^2} + \frac{p_{i,j,k-1} - 2p_{i,j,k} + p_{i,j,k+1}}{\Delta z^2} = f_{i,j,k}. \quad (8)$$

According to the boundary conditions, we apply corresponding type discrete Fourier transform (DFT) operators \mathcal{F} to equation (8) in x and y directions respectively, and then equation (8) is decoupled to a series of tridiagonal linear equations

$$\left(\frac{\lambda_i}{\Delta x^2} + \frac{\lambda_j}{\Delta y^2} \right) \hat{p}_{i,j,k} + \frac{1}{\Delta z^2} \left(\hat{p}_{i,j,k-1} + 2\hat{p}_{i,j,k} + \hat{p}_{i,j,k+1} \right) = \hat{f}_{i,j,k}, \quad (9)$$

where $\hat{\square} \equiv \mathcal{F}^y(\mathcal{F}^x(\square))$, λ_i and λ_j are eigenvalues. Actually, the operator \mathcal{F} could be applied a third time in z direction and thus equation (9) could be completely decoupled. However, considering that a nonuniform grid in z direction is common in the numerical simulation of wall turbulence, the Thomas algorithm should be a more flexible solution method to equation (9). Furthermore, the time complexity of the Thomas algorithm, $O(n)$, is better than that of the DFT algorithm, $O(n \log n)$. Hence, the Thomas algorithm is applied to solve the equation (9) efficiently. After that, we apply inverse DFT operators \mathcal{F}^{-1} to the solution in x and y directions respectively, and then the final numerical solution of the pressure Poisson equation can be obtained. Note, however, that the Thomas algorithm imposes a restriction on the domain decomposition, i.e., the computational domain should not be decomposed in z direction. From the discussion in Section 3 below, two additional all-to-all transpose communications are required to perform the Thomas algorithm in a 2D domain decomposition, which degrades the parallel performance to some extent. Hence, this paper adopts the highly efficient PDD algorithm with low communication overhead to solve the tridiagonal systems (9) in parallel.

2.2 The PDD algorithm

The following is a brief introduction to the PDD algorithm. Consider the following tridiagonal linear system:

$$Ax = d, \quad (10)$$

where A is a tridiagonal matrix of order n , $x = (x_1, \dots, x_n)^T$ and $d = (d_1, \dots, d_n)^T$. In order to solve equation (10) in parallel, the matrix A should be partitioned into p sub-matrices, where p is the number of partitions. For convenience, the order n is assumed to be exactly divisible by p , i.e., $n = pm$, where m is the size of a partition. The matrix A can be regarded as the superposition of the following two matrices

$$A = \tilde{A} + \Delta A, \quad (11)$$

where \tilde{A} is a block diagonal matrix with diagonal sub-matrices $A_i (i = 1, \dots, p)$ of order m , and the remaining elements (the entries with frame) make up ΔA , as illustrated in equation (12). Note that $\square_j^i = \square_{(i-1)*m+j}$. The vectors x and d are partitioned equally by p .

$$A = \left(\begin{array}{ccc} b_1^1 & c_1^1 & \\ a_2^1 & b_2^1 & c_2^1 \\ \ddots & \ddots & \ddots \\ & a_{m-1}^1 & b_{m-1}^1 & c_{m-1}^1 \\ & a_m^1 & b_m^1 & \boxed{c_m^1} \\ & \boxed{a_1^2} & b_1^2 & c_1^2 \\ & a_2^2 & b_2^2 & c_2^2 \\ & \ddots & \ddots & \ddots \\ & a_{m-1}^{p-1} & b_{m-1}^{p-1} & c_{m-1}^{p-1} \\ & a_m^{p-1} & b_m^{p-1} & \boxed{c_m^{p-1}} \\ & \boxed{a_1^p} & b_1^p & c_1^p \\ & a_2^p & b_2^p & c_2^p \\ & \ddots & \ddots & \ddots \\ & a_{m-1}^p & b_{m-1}^p & c_{m-1}^p \\ & a_m^p & b_m^p & \end{array} \right) \quad (12)$$

Let e_i be a column vector with its i th ($1 \leq i \leq n$) element being one and all the other entries being zero. The matrix ΔA can be written as

$$\Delta A = \left[a_{m+1}e_{m+1}, c_m e_m, \dots, a_{(p-1)*m+1}e_{(p-1)*m+1}, c_{(p-1)*m}e_{(p-1)*m} \right] \begin{bmatrix} e_m^T \\ e_{m+1}^T \\ \vdots \\ e_{(p-1)*m}^T \\ e_{(p-1)*m+1}^T \end{bmatrix} = V E^T, \quad (13)$$

where both V and E are $n \times 2(p-1)$ matrices. Hence, the matrix A can be factored into

$$A = \tilde{A} + V E^T. \quad (14)$$

In this way, equation (10) can be solved using the Sherman-Morrison-Woodbury formula^{29,30}, that is

$$x = A^{-1}d = (\tilde{A} + V E^T)^{-1}d = \tilde{A}^{-1}d - \tilde{A}^{-1}V(I + E^T \tilde{A}^{-1}V)^{-1}E^T \tilde{A}^{-1}d. \quad (15)$$

Let $Z = I + E^T Y$, then equation (15) can be solved step by step as follows

$$\tilde{A}\tilde{x} = d, \quad (16)$$

$$\tilde{A}Y = V, \quad (17)$$

$$Zy = E^T \tilde{x}, \quad (18)$$

$$x = \tilde{x} - Yy. \quad (19)$$

Since the coefficient matrix is the same, both equation (16) and equation (17) can be solved using the Thomas algorithm

$$A_i [\tilde{x}^i, v^i, w^i] = [d^i, a_1^i e_1, c_m^i e_m], (1 \leq i \leq p, a_1^1 = c_m^p = 0), \quad (20)$$

where v^i and w^i are potentially nonzero column vectors of the i th row block of the matrix Y . Here the length of column vector e is m . The solution can be performed completely in parallel.

The solution of equation (18) is the core of the PDD algorithm. The matrix Z has the following form

$$Z = \begin{pmatrix} 1 & w_m^1 & 0 & & & & \\ v_1^2 & 1 & 0 & \boxed{w_1^2} & & & \\ \boxed{v_m^2} & 0 & 1 & w_m^2 & 0 & & \\ \ddots & \ddots & \ddots & \ddots & \ddots & \ddots & \\ & \ddots & \ddots & \ddots & \ddots & \ddots & \\ 0 & v_1^{p-1} & 1 & 0 & \boxed{w_1^{p-1}} & & \\ & \boxed{v_m^{p-1}} & 0 & 1 & w_m^{p-1} & & \\ & 0 & v_1^p & 1 & & & \end{pmatrix}. \quad (21)$$

Sun et al.²⁷ points out that the magnitude of the last component of v^i , i.e. v_m^i , and the first component of w^i , i.e. w_1^i , may be smaller than machine accuracy when $p \ll n$ (e.g., $n/p \geq 50$), especially for diagonal dominant tridiagonal systems. In this case, v_m^i and w_1^i can be dropped (the entries with frame shown in equation (21)), and Z becomes a block diagonal system consisting of $(p - 1)$ independent 2×2 blocks. Hence, equation (18) can be solved efficiently in parallel, which leads to the highly efficiently PDD algorithm.

The PDD algorithm, using p processors, consists of the following steps:

1. Allocate A_i, d^i, a_1^i and c_m^i to the i th processor, where $1 \leq i \leq p$.
2. Solve equation (20) in parallel on p processors, using the Thomas algorithm.
3. Send \tilde{x}_1^i, v_1^i from the i th processor to the $(i - 1)$ th processor, where $2 \leq i \leq p$.

4. On the first $(p - 1)$ processors, solve the following equation in parallel using Cramer's Rule

$$\begin{pmatrix} 1 & w_m^i \\ v_1^{i+1} & 1 \end{pmatrix} \begin{bmatrix} y_1^i \\ y_2^i \end{bmatrix} = \begin{bmatrix} \tilde{x}_m^i \\ \tilde{x}_1^{i+1} \end{bmatrix}, (1 \leq i \leq p - 1), \quad (22)$$

where $y_j^i = y_{(i-1) \times 2 + j}$, $j = 1, 2$. Then send y_1^i from the i th processor to the $(i + 1)$ th processor.

5. Calculate equation (19) in parallel on all processors, and the final solution is obtained.

$$x^i = \tilde{x}^i - [v^i, w^i] \begin{bmatrix} y_1^{i-1} \\ y_2^i \end{bmatrix}, (1 \leq i \leq p, y_1^0 = y_2^p = 0). \quad (23)$$

It can be seen that only two sendrecv communications are required when using the PDD algorithm to solve a tridiagonal linear system, which contributes to the high parallel efficiency. The communication pattern is illustrated in Figure 3. It is pointed out in Ref.³¹ that for diagonally dominant tridiagonal systems, the PDD algorithm approximates the true solution to within machine accuracy when the size of parallel partitions satisfies certain requirements.

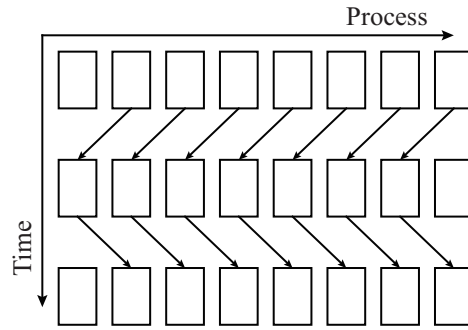


FIGURE 3 The communication pattern of the PDD algorithm²⁷.

3 Parallel strategy and implementation

Using an explicit time marching scheme, the update of velocity fields in the projection method is easy to parallelize. However, the global coupling of the pressure Poisson equation is often a critical challenge to massively parallel numerical simulations. Hence, this section focuses on the parallel strategy and the efficient implementation for the pressure Poisson equation.

3.1 Domain decomposition

Domain decomposition is one of the most important implementations of data parallelism in CFD. The computational domain for wall turbulence is usually a rectangular box. Three decomposition schemes are available, i.e. 1D plate-like decomposition, 2D pencil-like decomposition and 3D cube-like decomposition. The adoption of the final decomposition scheme should be considered carefully.

On the one hand, the parallel scalability and the communication overhead are affected by the decomposition. Consider the parallel decomposition of a cubic computational domain with periodic boundary conditions. The amount of computational work of each subdomain is proportional to the volume of itself, while the amount of communication required is proportional to the subdomain surface area. Then the computation-to-communication ratio, reflecting the parallel efficiency to some extent, roughly equals to the subdomain volume-to-area ratio. It should be maximized for good scalability and high parallel efficiency. It is not hard to find that both 2D pencil-like decomposition and 3D cube-like decomposition have a higher volume-to-area ratio, thus leading to less communication overhead and higher parallel efficiency.

On the other hand, the choice of decomposition is often limited by the adopted numerical method. The FFT calculation involved in solving the pressure Poisson equation is a global operation, which requires that each subdomain not be decomposed in the direction of transformation execution. If a 3D cube-like decomposition is adopted, then it should be reduced to a 2D pencil-like decomposition before performing FFTs, which results in extra overhead of data movement and communication.

From the above, a 2D pencil-like decomposition is chosen for the parallelization implementation of the numerical method, considering the trade-off between enhancing scalability and accommodating global algorithm features.

3.2 A parallel method for solving the pressure Poisson equation

The 2D FFT calculation in the horizontal directions is the first step to solve the pressure Poisson equation. Using a 2D pencil-like decomposition, FFTs in the long direction of the pencil-like subdomain can be performed in parallel. Hence, an x-pencil decomposition should be the initial decomposition to facilitate FFTs in x direction. Then an all-to-all global transpose from x-pencil decomposition to y-pencil decomposition is required to perform FFTs in y direction.

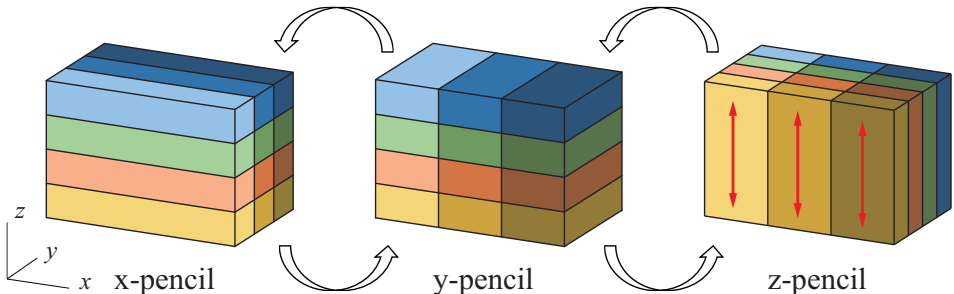


FIGURE 4 Illustration of 2D pencil-like domain decomposition and transpose in the process of solving the pressure Poisson equation using Thomas algorithm. The computational domain is decomposed into 3×4 subdomains, which is distinguished by a different color. The curved arrow indicates the transpose. The double-headed straight arrow indicates the solving process of Thomas algorithm.

After a forward 2D FFT, a series of tridiagonal linear equations merely coupled in z direction are obtained. However, due to the y-pencil decomposition at the moment, the equations cannot be solved directly using the Thomas algorithm. A common solution is to transpose y-pencil decomposition to z-pencil decomposition, ensuring all required data in z direction contained in each subdomain,

as illustrated in Figure 4. In this case, the whole solution requires four all-to-all global transposes. It is worth noting that the communication overhead of the all-to-all transpose is often expensive, in practice more time-consuming than the FFT operation. The transpose process will likely become a bottleneck of parallel performance in a massively parallel simulation. Hence, the PDD algorithm with low communication overhead is adopted to solve the tridiagonal systems in parallel, reducing two transposes between y-pencil decomposition and z-pencil decomposition. The solving process is illustrated in Figure 5.

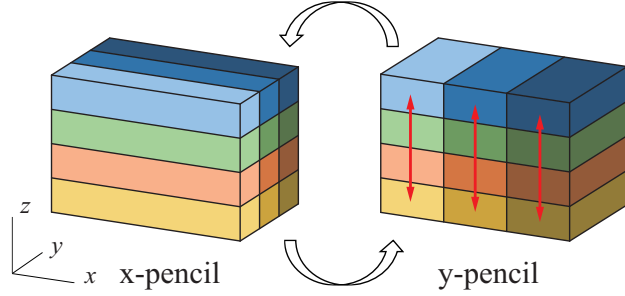


FIGURE 5 Illustration of 2D pencil-like domain decomposition and transpose in the process of solving the pressure Poisson equation using PDD algorithm. The double-headed straight arrow indicates the solving process of PDD algorithm.

In summary, the parallel method for solving the pressure Poisson equation is as follows:

- (1) Compute the right hand side (RHS) of the pressure Poisson equation, in x-pencil decomposition.
- (2) Perform forward 1D FFTs in x direction on the result of (1), in x-pencil decomposition.
- (3) Transpose the result of (2) from x-pencil decomposition to y-pencil decomposition.
- (4) Perform forward 1D FFTs in y direction on the result of (3), in y-pencil decomposition.
- (5) Solve the tridiagonal systems in parallel using the PDD algorithm, in y-pencil decomposition.
- (6) Perform forward 1D FFTs in y direction on the result of (5), in y-pencil decomposition.
- (7) Transpose the result of (6) from y-pencil decomposition to x-pencil decomposition.
- (8) Perform forward 1D FFTs in x direction on the result of (7), in x-pencil decomposition.

The method reduces the number of all-to-all transposes to two, and only introduces two sendrecv communications between neighboring subdomains, whose overhead is much smaller than that of all-to-all. Although the PDD algorithm requires some additional computation, the cost can be offset by the performance gains in communication.

3.3 Efficient implementation

The final parallel performance of the code depends not only on the parallel algorithm, but also on the implementation method. The code is developed in FORTRAN90/95. Considering that mainstream large-scale computing clusters all adopt a hybrid architecture of distributed memory and shared memory, the MPI/OpenMP hybrid programming model is utilized to give full play to the computing power of the machine and improve the parallel performance of the solver. The MPI process, corresponding with the decomposition subdomain, is responsible for calculation and communication at a coarse-grained parallel level. The OpenMP thread mainly implement fine-grained parallelization of the calculation part.

Communications between adjacent subdomains are necessary when calculating the spatial discretization for the convective, viscous, pressure terms, etc. For the second order centered finite difference adopted in this paper, the number of stencil points is three. Hence, an additional layer of halo cells should be set up around the subdomain to store a copy of boundary cells data of adjacent subdomains. Using 2D pencil-like decomposition, four pairwise data exchanges is required per halo update, which can be realized by calling the MPI_SENDRECV function.

Both FFT operation and data global transpose are critical steps of the parallel method for solving the pressure Poisson equation. In order to obtain good parallel performance, a multi-dimensional FFT and transpose module which supports MPI/OpenMP hybrid parallelism is developed by referring to the implementation of several open source libraries (e.g. PFFT¹⁸, P3DFFT¹⁹, 2DECOMP&FFT²⁰, etc.), which is highly efficient and scalable. Firstly, it is straight-forward to perform FFTs on batch data in parallel by using multiple threads, since the data lines to be transformed are independent of each other. It can be easily implemented by calling the multithreaded computing interface of general FFT libraries (e.g. FFTW³², MKL³³, etc.). Secondly, data reordering before and after the all-to-all transpose can also benefit from multithreaded parallelism. Take the transpose from x-pencil decomposition to y-pencil decomposition as an example, data reordering as shown in Figure 6 is required, before and after the all-to-all transpose. In other words, data sent to (or received from) different processes should be aggregated into a continuous memory buffer. The speed of this reordering is clearly limited by the memory bandwidth, as nothing but memory access is occurring. Note that data reordering is independent in z direction and can be processed in parallel using multiple threads, which can improve the memory bandwidth utilization by maintaining multiple data streams. Finally, the performance of the all-to-all communication mainly depends on the underlying implementation of the MPI library and the network architecture of the computing system. By adjusting communication parameters of the MPI library, the communication bandwidth can also be improved to some extent.

As for the parallel implementation of the PDD algorithm, the method of “batch calculation, batch communication” is adopted to reduce the communication overhead. After completing the forward 2D FFT calculation, adjacent processes in z direction need to jointly solve multiple (assuming n) mutually independent tridiagonal linear equations. If solutions are performed sequentially, on the one hand, $2n$ sendrecv communications are required according to the introduction of the PDD algorithm in Section 2. Since small messages are transmitted, the communication overhead is dominated by

the communication delay. On the other hand, it may also lead to a large number of strided memory accesses and reduce the computing performance. For this reason, the solution proposed in this paper is: each process uses multithreading to complete the pure computing tasks of solving tridiagonal systems at one time, aware of the locality principle. The calculation results are aggregated into a continuous memory buffer by using the derived datatype in MPI, and then transmitted in the form of large messages. This method can reduce the number of sendrecv communications to two, which minimizes the communication overhead and improves the communication bandwidth.

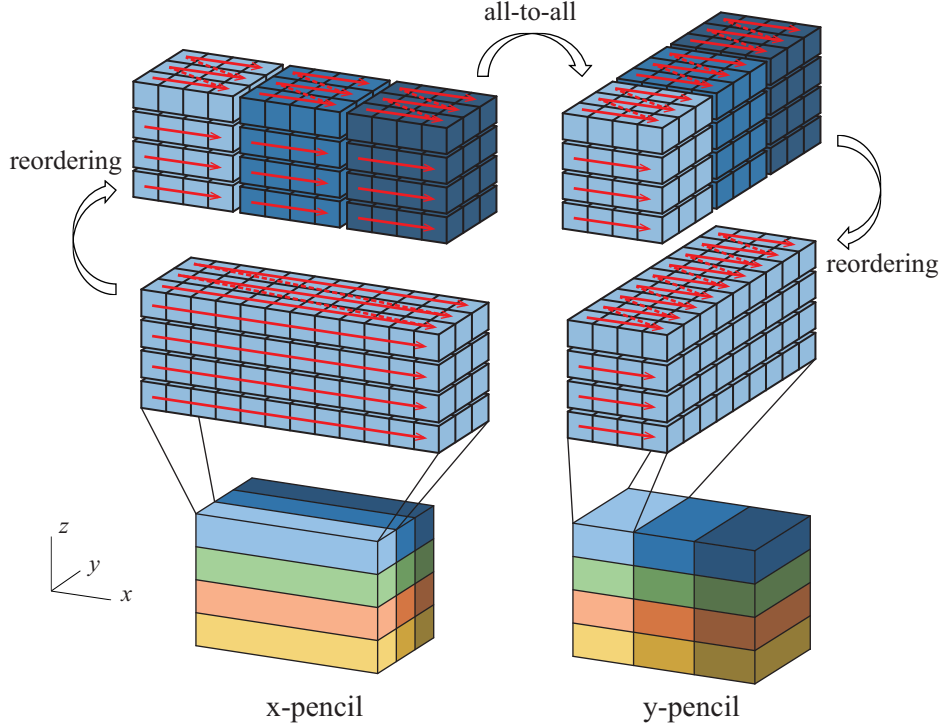


FIGURE 6 Illustration of data reordering in the transpose from x-pencil decomposition to y-pencil decomposition. The straight arrow and dotted line indicate the contiguous memory access order. Data sent to or received from different processes are distinguished by different colors.

3.4 PowerLLEL

From the above, several primary parallel strategies and optimizations are adopted to efficiently implement the proposed numerical method. The 2D pencil-like domain decomposition ensures the good scalability of the code, while the flexible MPI/OpenMP hybrid programming model speeds up not only the calculation of the momentum equation but also the PDD-based solution to the pressure Poisson equation. Finally, a new parallel solver for the 3D incompressible Navier-Stokes equations, PowerLLEL, is developed. It has the significant potential for massively parallel DNS of wall turbulence at a high Reynolds number and can be easily applied to the simulation of other incompressible flows.

4 Parallel performance

In this section, the parallel performance of PowerLLEL is presented through a series of strong and weak scalability tests. The performance difference between two parallel running modes, namely pure MPI and MPI/OpenMP hybrid, is also discussed. All tests are performed on the CPU partition of the Tianhe-2A supercomputer, currently ranked No. 6 in the world³⁴. Each computing node contains dual 12-core Intel Xeon E5-2692 v2 processors and 64 GB of memory. A dedicated network TH Express-2 based on the fat tree topology is adopted for node interconnection. The software environment for test is shown in Table 1. The grid configuration is shown in Table 2. Both in the strong and weak scalability tests (denoted by S and W respectively), two sets of grids of different sizes are used.

TABLE 1 Software environment for scalability tests.

Item	Name (version)
OS	Red Hat (6.5)
Compiler	Intel Fortran Compiler (14.0.2)
MPI Library	MPICH (3.1.3)
Math Library	FFTW (3.3.8)
IO Library	HDF5 (1.10.4)

TABLE 2 Grid configurations for scalability tests. Characters “S” and “W” in the item “Case” indicate the strong scalability test and weak scalability test, respectively. N_x , N_y , N_z are the number of points in x , y , z directions.

Case	N_x	N_y	N_z	Grid points
S1	2304	1536	864	3.06×10^9 (Total)
S2	4608	3072	1152	16.3×10^9 (Total)
W1	1152/2304/4608	768/1536/3072	864	2.65×10^6 (Per core)
W2	1536/3072/6144/9216	1152/2304/4608	864	5.31×10^6 (Per core)

As illustrated in Figure 7(a), PowerLLEL in MPI/OpenMP hybrid mode shows excellent strong scalability up to 9216 cores for a grid with 16.3 billion points, while it performs poor in pure MPI mode. The main reason is that as the number of CPU cores increases, the communication overhead in pure MPI mode increases faster, which leads to the decrease of parallel efficiency. In the case of weak scaling, the overall grid size becomes larger but the workload of each core remains the same. Linear scaling is achieved if the run time stays constant. Actually, the pure calculation time should be almost the same and only the increasing communication overhead will lead to the reduction of parallel efficiency. As shown in Figure 7(b), with the increase of cores, only a slight increase of the wall-clock time is observed in MPI/OpenMP hybrid mode, which suggests that PowerLLEL is able to solve a larger problem (i.e. higher Reynolds number) on a larger-scale system with a slight performance penalty. Moreover, the rapid increase of wall-clock time in pure MPI mode once again demonstrates that the communication overhead is the main reason for the relatively low parallel efficiency.

Finally, the absolute performance of PowerLLEL is also excellent. No matter in which mode, the wall-clock time per timestep of the code is very small, especially in the large-scale parallel numerical

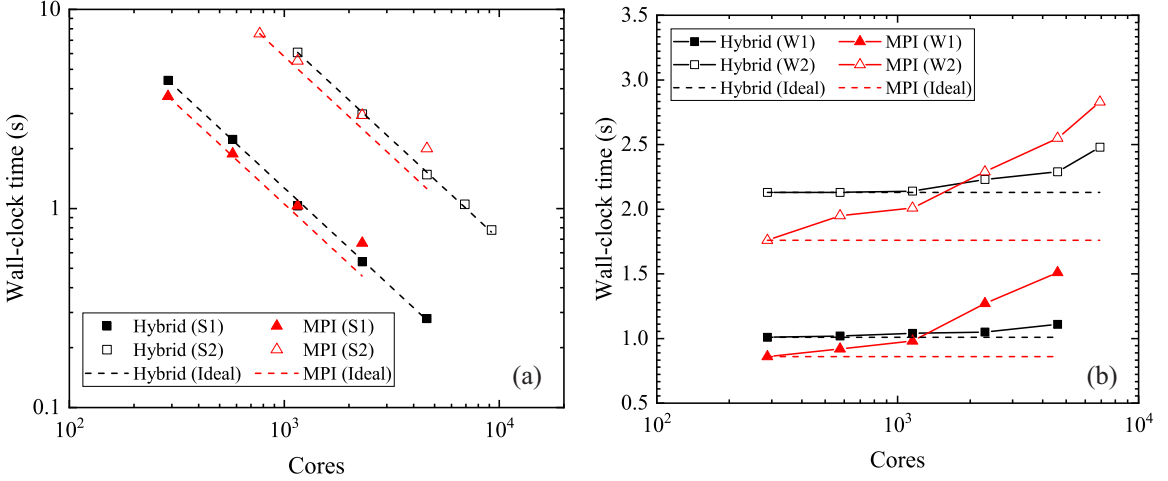


FIGURE 7 Strong (a) and weak (b) scalability tests for PowerLLEL. The dashed lines indicate the ideal scaling behavior. Performances in two parallel running modes, namely pure MPI and MPI/OpenMP hybrid, are labeled with red triangles and black squares respectively.

simulations. It is noteworthy that when the number of cores is small and the communication overhead has not become a bottleneck, the overall code performance in the pure MPI mode is better than that in the MPI/OpenMP hybrid mode.

5 Validation

TABLE 3 Summary of simulation parameters for turbulent channel flow cases. The initial letter of each case indicates the size of the domain: small (S), medium (M) and large (L). L_x and L_z are the computational domain sizes in the streamwise and spanwise directions. N_x, N_y, N_z are the number of grid points in the streamwise, wall-normal and spanwise directions. $\Delta x^+, \Delta y^+, \Delta z^+$ are the corresponding grid spacings. The statistical averaging time, T_{stat} , is given in terms of the eddy turn over time δ/u_τ .

Case	Re_τ	$L_x/\delta \times L_z/\delta$	$N_x \times N_y \times N_z$	Δx^+	Δz^+	Δy^+	$T_{\text{stat}}u_\tau/\delta$	Line style
L550	542	$4\pi \times 2\pi$	$1024 \times 360 \times 512$	6.65	6.65	0.20–7.63	8.13	— (black)
L1000	991	$4\pi \times 2\pi$	$2048 \times 540 \times 1024$	6.08	6.08	0.21–9.70	3.96	— (blue)
L2000	2003	$4\pi \times 2\pi$	$4096 \times 864 \times 2048$	6.14	6.14	0.23–12.6	3.41	— (red)
M550	542	$2\pi \times \pi$	$512 \times 360 \times 512$	6.65	3.32	0.15–6.35	10.75	— (black)
S1000	991	$\pi \times \pi/2$	$384 \times 600 \times 384$	8.11	4.05	0.17–6.96	11.89	— (blue)

To validate the simulation results of PowerLLEL, five new DNSs of the channel flow are carried out at friction Reynolds numbers $Re_\tau = u_\tau \delta / \nu = 550, 1000, 2000$, where $u_\tau = \sqrt{\tau_w / \rho}$ is the friction velocity, τ_w is the wall shear stress, δ is the channel half-height and ν is the kinematic viscosity coefficient. For the sake of convenience, x , y and z here indicate the streamwise, wall-normal and spanwise directions, respectively. Three simulations are computed in a large domain with streamwise and spanwise sizes of $L_x = 4\pi\delta$ and $L_z = 2\pi\delta$, while the other two use smaller boxes with $L_x = 2\pi\delta$, $L_z = \pi\delta$ and $L_x = \pi\delta$, $L_z = 0.5\pi\delta$, respectively. A minimal channel has been proved to provide correct one-point statistics and can be employed as an economical alternative to the costly large-

box channel flow DNS^{5,35,36}; this has also been verified here, indicating the reliable performance of PowerLLEL. Hence, the two small-box simulations can lay a foundation for DNS of channel flow at a higher Reynolds number. Uniform grids are used in the wall-parallel directions while a non-uniform grid clustered towards the wall is instead used in the wall-normal direction. Details on the grid configuration are provided in Table 3. The simulation of case L550 is initiated with a parabolic streamwise velocity profile with superposed random perturbations. The initial field of case L1000 at a higher Re_τ is interpolated from the fully developed field of case L550. The rest can be done in a similar fashion. Statistics are collected once the friction velocity u_τ reaches a statistically steady state. The reference data comes from the very recent simulations by Lee & Moser³, which has been shown to be with high quality via various means (see, for example, in Ref.³⁷). The lines in Table 3 are used consistently in later plots, unless otherwise stated.

Profiles of the mean streamwise velocity are shown in Figure 8(a). It can be seen that the DNS results in this paper are in good agreement with the reference data and present obviously a common logarithmic behavior for all the Reynolds numbers and box sizes. As presented in Figure 8(b)–8(d), the turbulent velocity fluctuation profiles also agree reasonably with the reference data, further illustrating that it is feasible to introduce the PDD-based approximate solver for the pressure Poisson equation to DNS of the channel flow.

The profiles of Reynolds shear stress at different Reynolds numbers are illustrated in Figure 8(e), in good agreement with the reference data. Note that it is believed for a long time that the peak location y_p^+ of $-\langle u'v' \rangle^+$ follows a $Re_\tau^{1/2}$ power law due to the logarithmic mean velocity profile. However, recent studies by Chen et al.³⁷ show that there is a scaling transition for the peak location (Figure 9(a)). That is, for small Re , the peak location is in the buffer layer rather than in the logarithmic layer, which thus nullifies the previous derivation of the $Re_\tau^{1/2}$ scaling (valid for large Re_τ). Instead, Chen et al.³⁷ presents an alternative $Re_\tau^{1/3}$ scaling for small Re_τ (less than 3000) based on the buffer layer eddies represented by the characteristic length function. In the Figure 9(a), we show our simulations together with previous DNS data, all in close agreement with the new $Re_\tau^{1/3}$ scaling, demonstrating well the quality of our simulations.

As for the streamwise turbulence intensity peak $\langle u'u' \rangle_p^+$, the existing explanations suggest a logarithmic growth with respect to Re_τ . Recently, Chen & Sreenivasan³⁸ propose an alternative formula for the peak magnitude that approaches a finite limit owing to the natural constraint of boundedness on the dissipation rate at the wall. As shown in Figure 9(b), our simulations together with previous DNS data of the channel flow validate this new formula.

In Figure 10, the budget of turbulent kinetic energy is plotted, comparing well with the reference data. All the cases show that the dominant balance is between production and dissipation away from the wall for $y^+ \gtrapprox 10$, while near the wall, it is the diffusion balancing the dissipation. Pressure transport is effective only in the domain $y^+ \lesssim 10$, and turbulent convection shows a positive energy gain for $y^+ \lesssim 7$ while redistributes energy outwards for larger y^+ . Note that all the productions show the maximum value 1/4 at $y^+ \approx 12$, which has been explained, e.g. in Cantwell³⁹. Moreover, towards the centerline, production becomes zero due to the vanishing mean shear and it is the convection

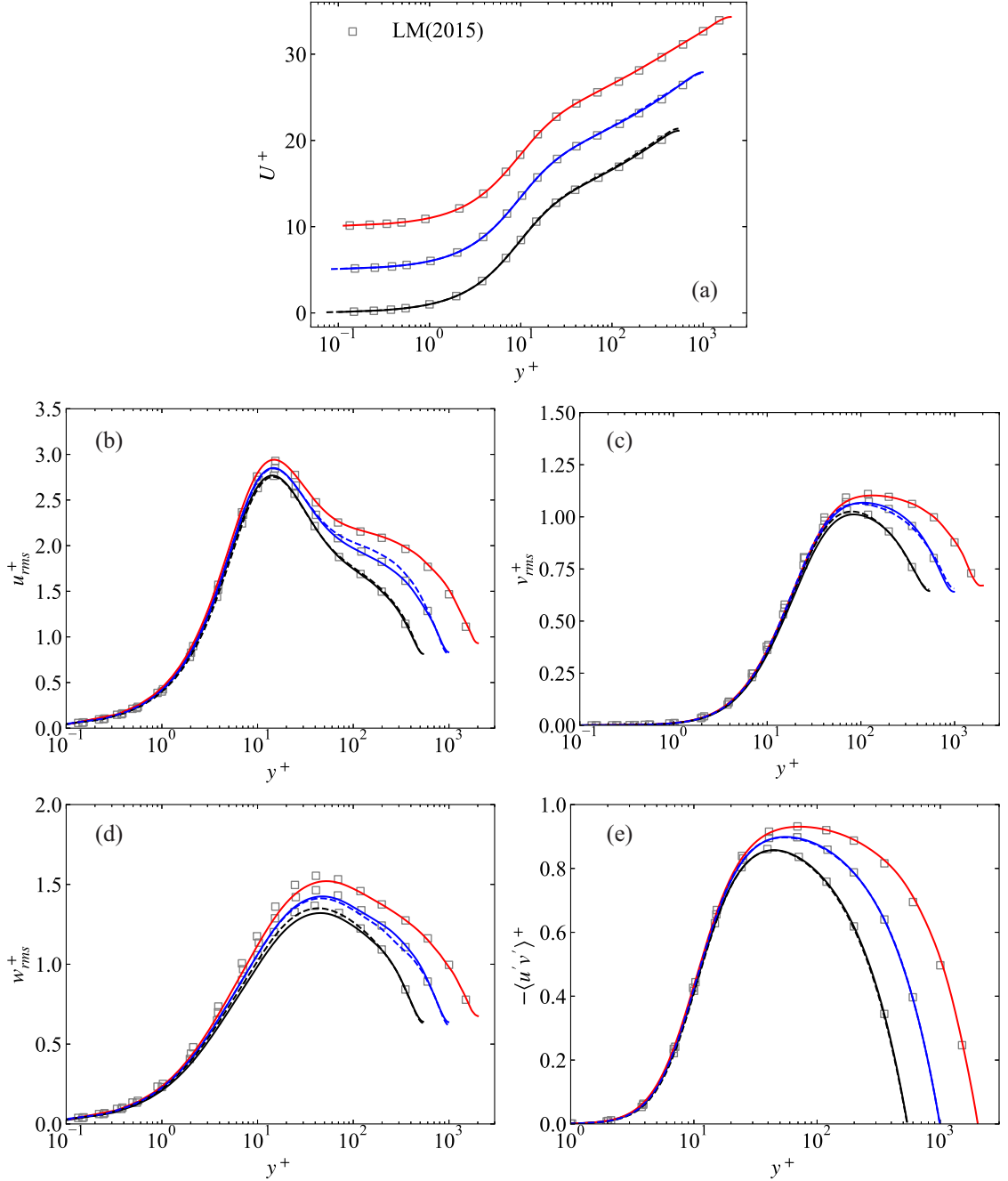


FIGURE 8 Profiles of the mean streamwise velocity (a), the turbulent velocity fluctuations (b, c, d) and the Reynolds shear stresses (e). Profiles of the mean streamwise velocity at $Re_\tau = 1000$ and $Re_\tau = 2000$ are offset by 5 and 10 units, respectively. Data from Lee et al.³ are marked with hollow squares, consistent in later plots unless otherwise stated. Lines are our simulations as specified in Table 3.

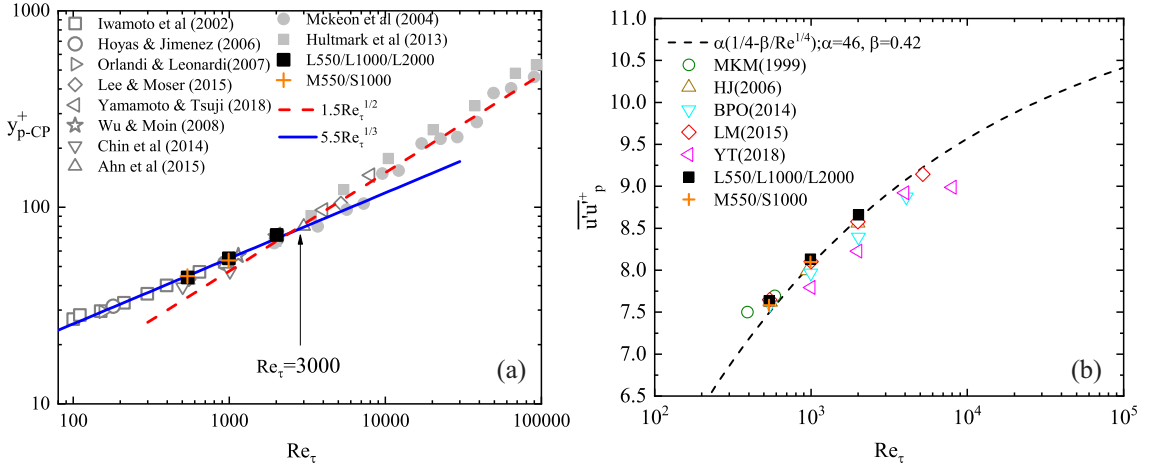


FIGURE 9 (a) Re-scaling of the peak location of $-\langle u'v' \rangle^+$; (b) Re-scaling of the streamwise turbulence intensity peak $\langle u'u' \rangle_p^+$. In (a), the solid line indicates the $Re_\tau^{1/3}$ scaling for small Re proposed by Chen et al.³⁷; the dashed line indicates the $Re_\tau^{1/2}$ scaling for high Re ; the grey symbols are previous DNS/experimental data compiled in Ref.³⁵; the solid squares indicate the present DNSs in a large box; the plus signs indicate the present DNSs in a smaller box. In (b), the dashed line indicates the Re scaling proposed by Chen et al.³⁸; the hollow symbols are previous DNS data of the channel flow^{4,10,6,3,11}.

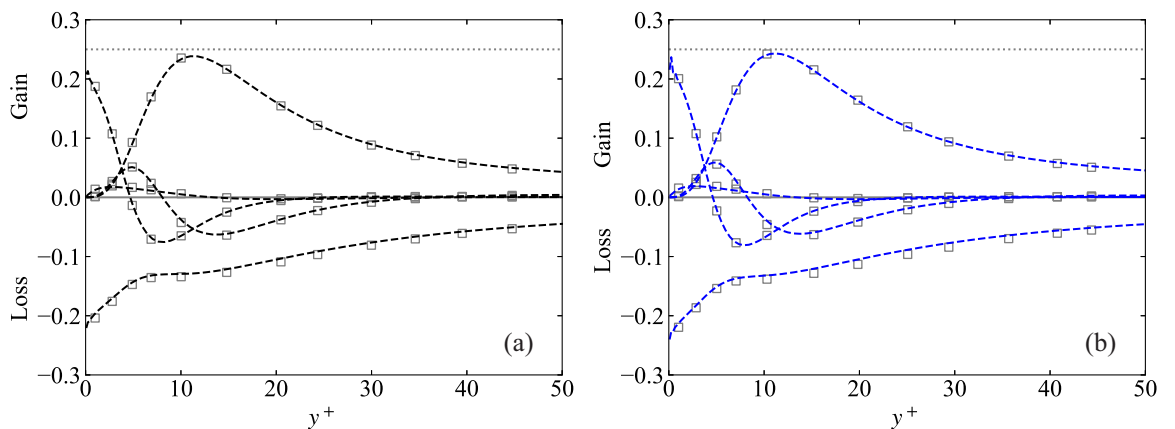


FIGURE 10 Budget of turbulent kinetic energy. (a) $Re_\tau = 550$; (b) $Re_\tau = 1000$. The position of $1/4$ is marked with a black dot-dashed line for reference.

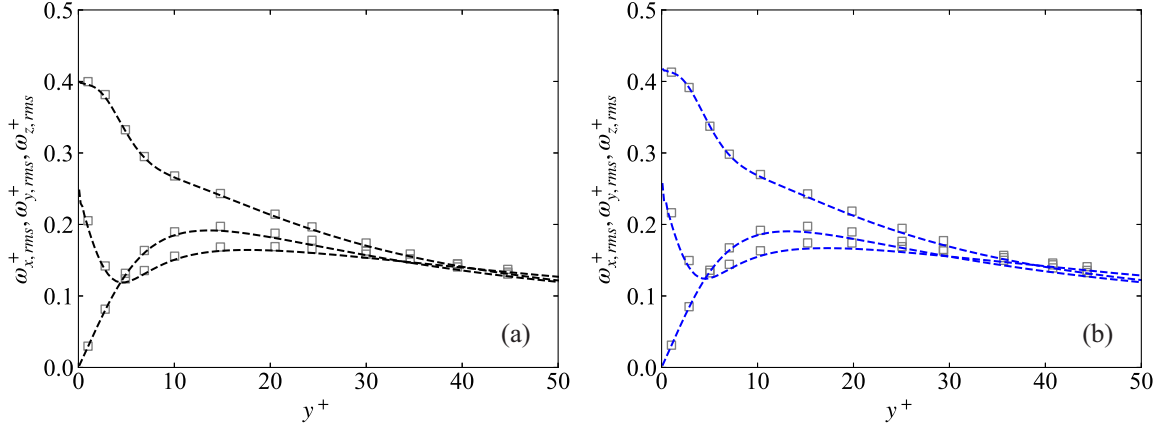


FIGURE 11 Profiles of root-mean-square (rms) of vorticity fluctuations. (a) $Re_\tau = 550$; (b) $Re_\tau = 1000$.

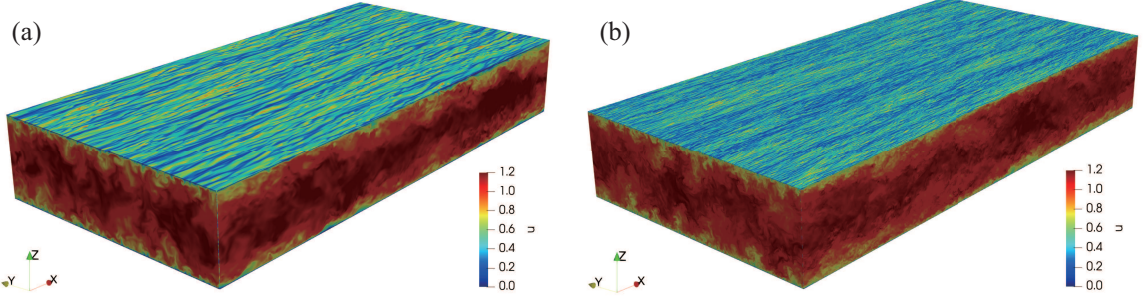


FIGURE 12 Instantaneous streamwise velocity for turbulent channel flow at $Re_\tau = 550$ (a) and $Re_\tau = 2000$ (b). The wall-parallel plane is at $y^+ = 10$.

balancing dissipation near the center⁴⁰; this is also observed in our simulations but not shown here.

The wall-normal dependence of vorticity fluctuations is shown in Figure 11. At the wall, $\omega_{y,rms}^+$ is zero due to the non-slip wall condition; $\omega_{z,rms}^+$ is the largest caused by the shear du/dy , and $\omega_{x,rms}^+$ is also nonzero due to the effect of streamwise vortices. Away from the wall, $\omega_{y,rms}^+$ increases rapidly due to the streaks ($du/dz \neq 0$), and for y^+ larger than 40, all the root-mean-square (rms) of vorticities are about the same value, indicating the turbulent flow is more isotropic than near the wall. In the above plots, our simulations are again in close agreement with the reference data.

Finally, Figure 12 shows a contour plot of the instantaneous streamwise velocity in a cross-stream, a streamwise and a wall-parallel plane at $y^+ = 10$. Low- and high-speed streaks, typical flow organization of incompressible wall turbulence, are distinctly shown in the wall-parallel plane. Sweep and ejection events can also be observed in the cross-stream plane. Compared to the case at $Re_\tau = 550$, there are more streaks distributed along the spanwise direction at $Re_\tau = 2000$; however, their average spacing $z^+ \approx 100$ is almost invariant, consistent with previous observations^{41,42}. Reducing the intensity of these streak structures would lead to a significant reduction of friction drag at the wall, as pursued by many recent studies⁴³.

6 Conclusions and prospects

In this paper, a highly efficient parallel method for solving the 3D incompressible Navier-Stokes equations is developed. The spatial discretization scheme is the standard second-order centered finite difference while an explicit second-order Runge-Kutta scheme is used for the time advancement. The core of the current method is an approximate solver for the pressure Poisson equation, which combines 2D FFTs with a highly efficient parallel approximate algorithm for tridiagonal systems, namely the PDD algorithm. Using a 2D pencil-like domain decomposition, only two all-to-all global communications and two sendrecv adjacent communications are involved in the process of solving the pressure Poisson equation in parallel. The proposed method is efficiently implemented in the MPI/OpenMP hybrid programming model and the 2D pencil-like domain decomposition, and a high-performance solver (i.e. PowerLLEL) is eventually developed. A series of the strong scalability tests have been carried out on the Tianhe-2A supercomputer. The results indicate that PowerLLEL in the MPI/OpenMP hybrid mode shows excellent strong scalability up to 10^4 cores when the number of grid points is 16.3 billion, and the wall-clock time per timestep is very small. Several direct numerical simulations of the channel flow at different friction Reynolds numbers ($Re_\tau = 550, 1000, 2000$) have been performed to validate the reliability of the proposed method, showing good agreement with reference data. With the help of the proposed method and PowerLLEL, it is possible to carry out massively parallel DNS of wall turbulence at higher Reynolds number with relatively low computational cost will be performed in future.

Note that PowerLLEL can also be applied for DNS of other incompressible flows (e.g. turbulent boundary layer, pipeline flow, etc.). Combined with the immerse boundary method, it is capable to simulate flows with complex boundary conditions (such as the simulation of boundary layer with surface roughness), to be pursued in future. Finally, it is our next goal to migrate PowerLLEL from pure CPU systems to the CPU-GPU heterogeneous systems.

Acknowledgments

This work was supported by the Fundamental Research Funds for the Central Universities, Sun Yat-sen University under Grant No. 19lgzd15 and the Science and Technology Project of Shenzhen under Grant No. JCYJ20190807160413162.

Disclosure statement

No potential conflict of interest was reported by the author(s).

References

1. Abide S, Binous MS, Zeghami B. An efficient parallel high-order compact scheme for the 3D incompressible Navier-Stokes equations. *International Journal of Computational Fluid Dynamics* 2017; 31(4-5): 214-229. doi: [10.1080/10618562.2017.1326592](https://doi.org/10.1080/10618562.2017.1326592)
2. Moon H, Hong S, You D. Application of the parallel diagonal dominant algorithm for the incompressible Navier-Stokes equations. *Journal of Computational Physics* 2020; 423. doi: [10.1016/j.jcp.2020.109795](https://doi.org/10.1016/j.jcp.2020.109795)
3. Lee M, Moser RD. Direct numerical simulation of turbulent channel flow up to $Re_\tau \approx 5200$. *Journal of Fluid Mechanics* 2015; 774: 395–415. doi: [10.1017/jfm.2015.268](https://doi.org/10.1017/jfm.2015.268)
4. Moser RD, Kim J, Mansour NN. Direct numerical simulation of turbulent channel flow up to $Re_\tau = 590$. *Physics of Fluids* 1999; 11(4): 943–945. doi: [10.1063/1.869966](https://doi.org/10.1063/1.869966)
5. Lozano-Durán A, Jiménez J. Effect of the computational domain on direct simulations of turbulent channels up to $Re_\tau = 4200$. *Physics of Fluids* 2014; 26(1): 011702. doi: [10.1063/1.4862918](https://doi.org/10.1063/1.4862918)
6. Bernardini M, Pirozzoli S, Orlandi P. Velocity statistics in turbulent channel flow up to $Re_\tau = 4000$. *Journal of Fluid Mechanics* 2014; 742: 171–191. doi: [10.1017/jfm.2013.674](https://doi.org/10.1017/jfm.2013.674)
7. Fadlun EA, Verzicco R, Orlandi P, Mohd-Yusof J. Combined immersed-boundary finite-difference methods for three-dimensional complex flow simulations. *Journal of Computational Physics* 2000; 161(1): 35–60. doi: <https://doi.org/10.1006/jcph.2000.6484>
8. Vreman AW, Kuerten JGM. Comparison of direct numerical simulation databases of turbulent channel flow at $Re_\tau = 180$. *Physics of Fluids* 2014; 26(1): 015102. doi: [10.1063/1.4861064](https://doi.org/10.1063/1.4861064)
9. Kim J, Moin P, Moser R. Turbulence statistics in fully developed channel flow at low reynolds number. *Journal of Fluid Mechanics* 1987; 177: 133–166. doi: [10.1017/S0022112087000892](https://doi.org/10.1017/S0022112087000892)
10. Hoyas S, Jiménez J. Scaling of the velocity fluctuations in turbulent channels up to $Re_\tau = 2003$. *Physics of Fluids* 2006; 18(1): 011702. doi: [10.1063/1.2162185](https://doi.org/10.1063/1.2162185)
11. Yamamoto Y, Tsuji Y. Numerical evidence of logarithmic regions in channel flow at $Re_\tau = 8000$. *Physical Review Fluids* 2018; 3(1): 012602. doi: [10.1103/PhysRevFluids.3.012602](https://doi.org/10.1103/PhysRevFluids.3.012602)
12. Gholami A, Malhotra D, Sundar H, Biros G. FFT, FMM, or Multigrid? A comparative study of State-Of-the-Art Poisson solvers for uniform and nonuniform grids in the unit cube. *SIAM Journal on Scientific Computing* 2016; 38(3): C280–C306. doi: [10.1137/15m1010798](https://doi.org/10.1137/15m1010798)
13. Schumann U, Sweet RA. Fast Fourier transforms for direct solution of poisson's equation with staggered boundary conditions. *Journal of Computational Physics* 1988; 75(1): 123–137. doi: [https://doi.org/10.1016/0021-9991\(88\)90102-7](https://doi.org/10.1016/0021-9991(88)90102-7)

14. van der Poel EP, Ostilla-Mónico R, Donners J, Verzicco R. A pencil distributed finite difference code for strongly turbulent wall-bounded flows. *Computers & Fluids* 2015; 116: 10–16. doi: <https://doi.org/10.1016/j.compfluid.2015.04.007>
15. Zhu X, Phillips E, Spandan V, et al. AFiD-GPU: A versatile Navier-Stokes solver for wall-bounded turbulent flows on GPU clusters. *Computer Physics Communications* 2018; 229: 199–210. doi: <https://doi.org/10.1016/j.cpc.2018.03.026>
16. Ostilla-Mónico R, Verzicco R, Grossmann S, Lohse D. The near-wall region of highly turbulent Taylor-Couette flow. *Journal of Fluid Mechanics* 2016; 788: 95–117. doi: [10.1017/jfm.2015.675](https://doi.org/10.1017/jfm.2015.675)
17. Costa P. A FFT-based finite-difference solver for massively-parallel direct numerical simulations of turbulent flows. *Computers & Mathematics with Applications* 2018; 76(8): 1853–1862. doi: <https://doi.org/10.1016/j.camwa.2018.07.034>
18. Pippig M. PFFT: An extension of FFTW to massively parallel architectures. *SIAM Journal on Scientific Computing* 2013; 35(3): C213–C236. doi: [10.1137/120885887](https://doi.org/10.1137/120885887)
19. Pekurovsky D. P3DFFT: A framework for parallel computations of Fourier transforms in three dimensions. *SIAM Journal on Scientific Computing* 2012; 34(4): C192–C209. doi: [10.1137/11082748x](https://doi.org/10.1137/11082748x)
20. Li N, Laizet S. 2DECOMP&FFT — A highly scalable 2D decomposition library and FFT interface. In: Cray User Group. ; 2010.
21. Duy TVT, Ozaki T. A decomposition method with minimum communication amount for parallelization of multi-dimensional FFTs. *Computer Physics Communications* 2014; 185(1): 153–164. doi: <https://doi.org/10.1016/j.cpc.2013.08.028>
22. Song S, Hollingsworth JK. Computation-communication overlap and parameter auto-tuning for scalable parallel 3-D FFT. *Journal of Computational Science* 2016; 14: 38–50. doi: [10.1016/j.jocs.2015.12.001](https://doi.org/10.1016/j.jocs.2015.12.001)
23. Stone HS. An Efficient Parallel Algorithm for the Solution of a Tridiagonal Linear System of Equations. *J. ACM* 1973; 20(1): 27–38. doi: [10.1145/321738.321741](https://doi.org/10.1145/321738.321741)
24. Hockney RW. A fast direct solution of Poisson's equation using Fourier analysis. *J. ACM* 1965; 12(1): 95–113. doi: [10.1145/321250.321259](https://doi.org/10.1145/321250.321259)
25. Lawrie DH, Sameh AH. The computation and communication complexity of a parallel banded system solver. *ACM Trans. Math. Softw.* 1984; 10(2): 185–195. doi: [10.1145/399.401](https://doi.org/10.1145/399.401)
26. Wang HH. A parallel method for tridiagonal equations. *ACM Trans. Math. Softw.* 1981; 7(2): 170–183. doi: [10.1145/355945.355947](https://doi.org/10.1145/355945.355947)

27. Sun XH, Sun HZ, Ni LM. Parallel algorithms for solution of tridiagonal systems on multicomputers. In: ICS '89. Association for Computing Machinery. Association for Computing Machinery; 1989; New York, NY, USA: 303–312
28. Bao Y, Luo J, Ye M. Parallel Direct Method of DNS for Two-Dimensional Turbulent Rayleigh-Bénard Convection. *Journal of Mechanics* 2017; 34(2): 159-166. doi: [10.1017/jmech.2017.54](https://doi.org/10.1017/jmech.2017.54)
29. Sherman J, Morrison WJ. Adjustment of an inverse matrix corresponding to a change in one element of a given matrix. *Ann. Math. Statist.* 1950; 21(1): 124–127. doi: [10.1214/aoms/1177729893](https://doi.org/10.1214/aoms/1177729893)
30. Woodbury MA. *Inverting modified matrices*. Princeton, NJ: Department of Statistics, Princeton University . 1950.
31. Sun XH. Application and accuracy of the parallel diagonal dominant algorithm. *Parallel Computing* 1995; 21(8): 1241–1267. doi: [https://doi.org/10.1016/0167-8191\(95\)00018-J](https://doi.org/10.1016/0167-8191(95)00018-J)
32. Frigo M, Johnson SG. The design and implementation of FFTW3. *Proceedings of the IEEE* 2005; 93(2): 216–231. doi: [10.1109/JPROC.2004.840301](https://doi.org/10.1109/JPROC.2004.840301)
33. Intel . Intel Math Kernel Library. <https://software.intel.com/content/www/us/en/develop/> 2020.
34. TOP500. <https://www.top500.org/lists/top500/2020/11>; 2020.
35. Flores O, Jiménez J. Hierarchy of minimal flow units in the logarithmic layer. *Physics of Fluids* 2010; 22(7): 071704. doi: [10.1063/1.3464157](https://doi.org/10.1063/1.3464157)
36. Jiménez J, Moin P. The minimal flow unit in near-wall turbulence. *Journal of Fluid Mechanics* 1991; 225: 213–240. doi: [10.1017/S0022112091002033](https://doi.org/10.1017/S0022112091002033)
37. Chen X, Hussain F, She Z. Non-universal scaling transition of momentum cascade in wall turbulence. *Journal of Fluid Mechanics* 2019; 871. doi: [10.1017/jfm.2019.309](https://doi.org/10.1017/jfm.2019.309)
38. Chen X, Sreenivasan KR. Reynolds number scaling of the peak turbulence intensity in wall flows. *Journal of Fluid Mechanics* 2020; 908. doi: [10.1017/jfm.2020.991](https://doi.org/10.1017/jfm.2020.991)
39. Cantwell BJ. A universal velocity profile for smooth wall pipe flow. *Journal of Fluid Mechanics* 2019; 878: 834–874. doi: [10.1017/jfm.2019.669](https://doi.org/10.1017/jfm.2019.669)
40. Chen X, Hussain F, She Z. Quantifying wall turbulence via a symmetry approach. Part 2. Reynolds stresses. *Journal of Fluid Mechanics* 2018; 850: 401–438. doi: [10.1017/jfm.2018.405](https://doi.org/10.1017/jfm.2018.405)
41. Marusic I, McKeon BJ, Monkewitz PA, Nagib HM, Smits AJ, Sreenivasan KR. Wall-bounded turbulent flows at high Reynolds numbers: Recent advances and key issues. *Physics of Fluids* 2010; 22(6): 065103. doi: [10.1063/1.3453711](https://doi.org/10.1063/1.3453711)

42. Jiménez J. Cascades in wall-bounded turbulence. *Annual Review of Fluid Mechanics* 2012; 44(1): 27–45. doi: [10.1146/annurev-fluid-120710-101039](https://doi.org/10.1146/annurev-fluid-120710-101039)
43. Yao J, Chen X, Hussain F. Drag control in wall-bounded turbulent flows via spanwise opposed wall-jet forcing. *Journal of Fluid Mechanics* 2018; 852: 678–709. doi: [10.1017/jfm.2018.553](https://doi.org/10.1017/jfm.2018.553)